Deutsche Ausgabe: DOI: 10.1002/ange.201706895
Internationale Ausgabe: DOI: 10.1002/anie.201706895

Cove-Edge Nanoribbon Materials for Efficient Inverted Halide Perovskite Solar Cells

Edison Castro[+], *Thomas J. Sisto*[+], *Elkin L. Romero, Fang Liu, Samuel R. Peurifoy, Jue Wang, Xiaoyang Zhu, Colin Nuckolls,* and Luis Echegoyen**

Abstract: *Two cove-edge graphene nanoribbons hPDI2-Pyr-hPDI2 (**1**) and hPDI3-Pyr-hPDI3 (**2**) are used as efficient electron-transporting materials (ETMs) in inverted planar perovskite solar cells (PSCs). Devices based on the new graphene nanoribbons exhibit maximum power-conversion efficiencies (PCEs) of 15.6 % and 16.5 % for **1** and **2**, respectively, while a maximum PCE of 14.9 % is achieved with devices based on [6,6]-phenyl-C_{61}-butyric acid methyl ester ($PC_{61}BM$). The interfacial effects induced by these new materials are studied using photoluminescence (PL), and we find that **1** and **2** act as efficient electron-extraction materials. Additionally, compared with $PC_{61}BM$, these new materials are more hydrophobic and have slightly higher LUMO energy levels, thus providing better device performance and higher device stability.*

Herein, we describe the first use of graphene nanoribbons as the electron-transporting layer in PSCs, leading to increased device performance compared to widely used $PC_{61}BM$. Since their introduction in 2008, hybrid organic–inorganic perovskite materials have shown great promise as the active layer in photovoltaic cells. Because of their efficient light absorption and low cost, lead halide perovskites ($CH_3NH_3PbX_3$; X = I, Br, Cl) have become high performance materials that have the potential to fulfill the requirements for the large-scale deployment of solar energy.[1,2] Recently, there has been great interest in these materials, leading to remarkable increases in photoconversion efficiency, from 3.8 % in 2009 to 22.1 % in 2016.[3,4] One area of focus for improving PSCs are the hole- and electron-extracting layers that encapsulate the active layer. These layers are invaluable because they determine the polarity of the device, improve stability, passivate surface charge traps, and aid in charge-extraction transport from the active layer to the electrodes (Figure 1).[5,6]

To date, PSCs based on both *meso*-superstructure[7] and planar device structures[8] have achieved PCEs over 20 %. Despite the lower PCE at present, the inverted planar devices, which are based on p-i-n configurations, are attractive because the relatively simple device architecture is promising for flexible devices and is amenable to low-temperature and scalable fabrication techniques.[9,10] There are many hole transporting materials (HTMs) suitable for this type of solar cells. For example, poly(3,4-ethylenedioxythiophene):poly(styrenesulfonate) (PEDOT:PSS), NiO_x, CuI, and CuSCN are all commonly used.[11] However, the ETM is limited mainly to fullerenes such as $PC_{61}BM$ and other derivatives,[12–17] and there are few examples of efficient non-fullerene inverted PSCs reported.[18–21] To further enhance PSCs, new ETMs must be developed and studied.

Herein, we report that two atomically precise edge-functionalized graphene nanoribbons hPDI2-Pyr-hPDI2 (**1**) and hPDI3-Pyr-hPDI3 (**2**) outperform $PC_{61}BM$ as ETMs in PSCs, with average PCEs of 14.9 ± 0.7 % and 15.9 ± 0.6 % for **1** and **2**, respectively, as compared to 14.2 ± 0.7 % for $PC_{61}BM$ (Figure 1). These soluble, electron-poor ribbons provide a facile fabrication process, high electron mobility, strong light absorption, and HOMO/LUMO levels that match those of the lead-halide perovskite active layers.[22,23] This is the first example of graphene nanoribbons being used as the transport layer in PSCs, and points to the promise of functionalized graphene for the enhancement of the transport layers of solar cells.

Recently, some of us reported the bottom-up synthesis of edge-functionalized graphene nanoribbons **1** and **2**, and their materials characterization as ETMs.[23] Notably, the cyclic voltammograms of **1** and **2** showed multiple reduction events that prompted us to explore the electrochemistry of these nanoribbons further for their use as the ETMs in PSCs. It is vital for an electron-transport layer to have a LUMO that is well matched with the active layer to aid in electron extraction, as well as a HOMO that is low enough to block hole transport. Estimates of the HOMO/LUMO values from cyclic voltammetry (CV) reveal that the nanoribbons **1** and **2** fulfill these requirements. The energy level diagrams of **1** and **2** are represented in Figure 1 b, and the estimated LUMO of **1** and **2** are located at −3.7 eV and −3.8 eV, respectively. Both ribbons' LUMO levels match the conduction band of the perovskite (−3.7 eV).[24] The HOMO energy levels of **1** and **2** are both −5.8 eV, much deeper than the valence band of the perovskite (−5.4 eV),[24] and thereby should provide efficient hole-blocking ability.

To test the hypothesis that these ribbons would be effective in PSCs, we fabricated devices using **1**, **2**, and

---

[*] E. Castro,[+] E. L. Romero, Prof. L. Echegoyen
Department of Chemistry, University of Texas at El Paso
El Paso, TX, 79968 (USA)
E-mail: echegoyen@utep.edu

Dr. T. J. Sisto,[+] F. Liu, S. R. Peurifoy, J. Wang, Prof. X. Zhu,
Prof. C. Nuckolls
Department of Chemistry, Columbia University
New York, NY, 10027 (USA)
E-mail: cn37@columbia.edu

[+] These authors contributed equally to this work.

Supporting information and the ORCID identification number(s) for the author(s) of this article can be found under: https://doi.org/10.1002/anie.201706895.

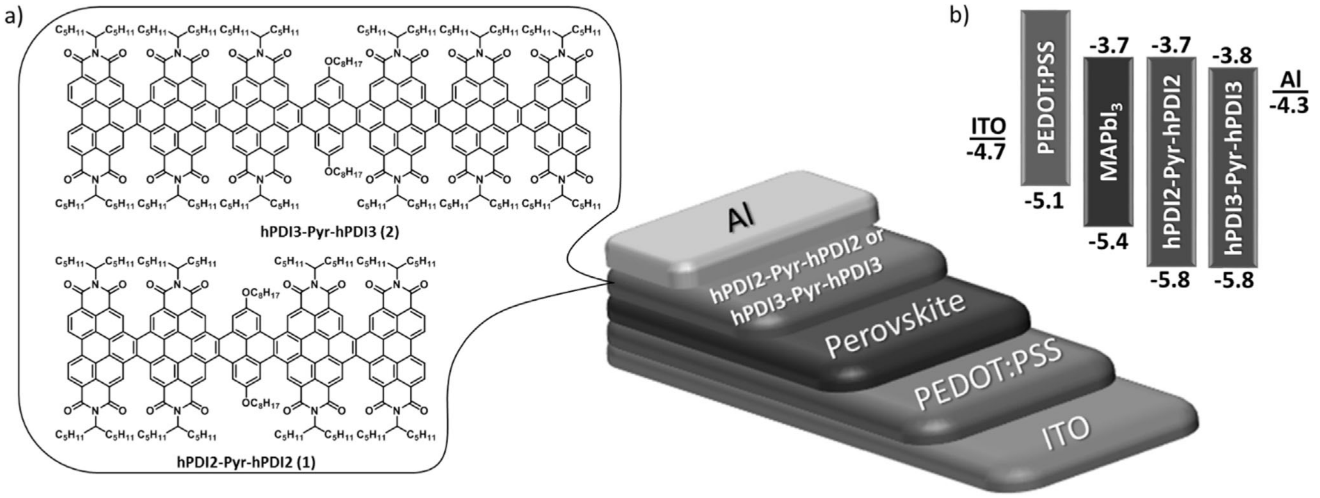

Figure 1. a) Device structure of the inverted PSC using hPDI2-Pyr-hPDI2 (**1**) or hPDI3-Pyr-hPDI3 (**2**) as the ETMs. b) Schematic of the estimated HOMO/LUMO energy levels.[23,24]

$PC_{61}BM$. The current–voltage (*J*–*V*) curves of these devices using inverted planar structures are shown in Figure 2a. The photovoltaic parameters of the devices are summarized in Table 1.

The highest PCEs for devices based on **1** and **2** as ETMs were 15.6% and 16.5%, respectively. The efficiencies are higher than those of devices based on $PC_{61}BM$, which yielded a highest PCE of 14.9% under the same conditions. The external quantum efficiency (EQE) spectra (Supporting Information, Figure S1) were higher for ribbon **2** based devices, and the integrated J_{sc} is in agreement with the values obtained from the *J*–*V* values (Table 1). The higher J_{sc} values obtained from devices based on **2** can be attributed to the slightly higher electron mobility of this compound. The higher V_{oc} values obtained from both **1** and **2** compared with that of the $PC_{61}BM$ can be associated with the higher LUMO levels of the two ribbons.[25] To investigate the hysteresis behavior, devices were tested in both forward and reverse scan directions. As shown in Figure 2b, devices based on the two ribbons displayed relatively consistent *J*–*V* curves, independent of the scan direction, indicating a negligible hysteresis effect in the PSCs.

To further verify device efficiencies, the maximal steady-state power outputs were monitored and plotted as a function of time. As shown in Figure 2c, devices based on **1** and **2** at 0.78 V resulted in 19.85 $mA\,cm^{-2}$ and 20.95 $mA\,cm^{-2}$, yielding PCEs of 15.5% and 16.3%, respectively. Statistical histograms of PCEs from 15 individual devices using **1**, **2**, and $PC_{61}BM$ as the ETMs are shown in Figure 2d. The distribution exhibited average efficiencies of 14.9 ± 0.7%, 15.9 ± 0.6%, and 14.2 ± 0.7% for **1**-, **2**-, and $PC_{61}BM$-based devices, respectively.

To understand the efficiency of transport through the electron-transport layer, the electron mobilities of **1**, **2**, and $PC_{61}BM$ were obtained from space-charge-limited current (SCLC) experiments. The mobilities of all three devices were similar ($10^{-4}\,cm^2\,V^{-1}\,s^{-1}$),[13,23] which shows that the two ribbons conduct as efficiently as $PC_{61}BM$.

To study recombination losses and the role of the two ribbons as the electron-transport layers, steady-state PL and time-resolved (TR-PL) decay measurements were recorded for perovskite, perovskite/**1**, perovskite/**2**, and for perovskite/$PC_{61}BM$ films as shown in Figure 2e. When the perovskite layer forms a contact with **1**, **2**, or $PC_{61}BM$, a significant PL-quenching effect was observed, indicating that all of the extracting layers are efficiently inhibiting electron-hole recombination.[26] As ribbon **1** and ribbon **2** exhibit pronounced PL between 600–750 nm,[23] the passivation effect was not clearly observed in the steady-state PL. As shown in Figure 2f, shorter PL decay times were observed for perovskite/ETMs (0.9, 0.9, and 1 ns for perovskite/**1**, perovskite/**2**, and perovskite/$PC_{61}BM$, respectively) than that of only perovskite (3 ns). The shortened decay lifetime observed with all of the electron-transport layers shows fast extraction and transport of charge carriers, which suppresses electron-hole recombination and increases the J_{sc}.[27]

In addition to the energy levels, the CV of **1** and **2** in THF (Supporting Information, Figure S2; Table 2) show four and six reversible reduction events grouped in pairs, respectively. We became interested in quantifying how many electrons were added to **1** and **2** for each of these reduction events. It is well known from other perylene diimide (PDI) oligomers that each PDI subunit accepts two electrons. If this is also the case for **1** and **2**, then **1** reversibly accepts 8 electrons, while **2** reversibly accepts a remarkable 12 electrons. To confirm this, controlled potential electrolysis of **1** and **2** in THF containing 0.1 M $TBAPF_6$ was performed at a potential circa 60 mV more negative than each reduction potential (see Figure S2, arrows).

The stoichiometry of the charge (coulombs) transferred corresponded to two electrons per molecule for each reduction wave. Moreover, the anions showed no decomposition and were very stable under these conditions (Table 3). Subsequent re-oxidation at 0 V showed regeneration of the neutral species with no change in the CV nor in the Osteryoung square-wave voltammetry, indicating that each process is completely chemically reversible. These results

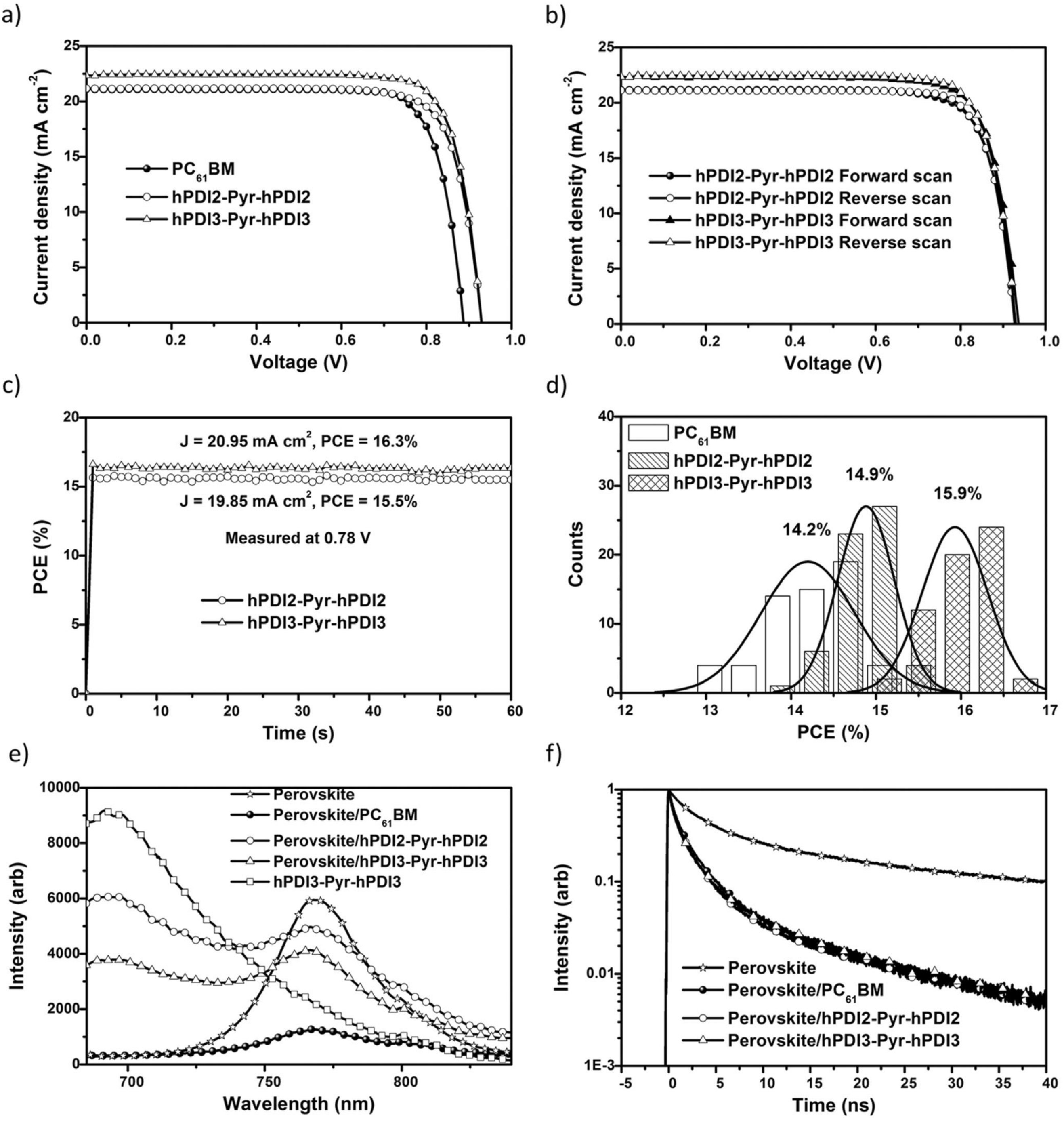

Figure 2. a) *J–V* curves measured under 1 sun illumination (100 mW cm^{-2}, AM 1.5 G). b) *J–V* curves under 1 sun illumination in forward and reverse voltage scans. c) Power output under maximum power point tracking for 60 s, resulting in a stabilized power output of 15.5% and 16.3% (at 0.78 V) when **1** and **2** were used as the ETMs, respectively. d) The PCE histograms measured for 15 independent devices. e) Steady-state PL spectra of the perovskite and perovskite/ETM films. f) TR-PL spectra of the perovskite and perovskite/ETM films.

Table 1: Summary of performance of devices based on **1**, **2**, and PC$_{61}$BM.

ETM	J_{sc} [mA cm^{-2}][a]	J_{sc} [mA cm^{-2}]	V_{oc} [V]	FF [%]	PCE (%)
PC$_{61}$BM	21.08	21.10	0.88	0.80	14.2 ± 0.7 (14.9)
1	21.18	21.17	0.93	0.79	14.9 ± 0.7 (15.6)
2	22.66	22.68	0.93	0.78	15.9 ± 0.6 (16.5)

[a] *Calculated current, highest PCE in parentheses. The average was calculated from 15 devices.

Table 2: Cyclic voltammetric results for **1** and **2** obtained in THF + 0.1 M TBAPF$_6$.

Compound	Redox potentials (in V versus Fc$^+$/Fc)					
	I	II	III	IV	V	VI
1	−1.26	−1.44	−1.79	−1.92	–	–
2	−1.05	−1.21	−1.38	−1.58	−1.76	−1.89

Table 3: CPE of **1** and **2** in THF + 0.1 M $TBAPF_6$.

Compound	1		2	
	Red.	Ox.	Red.	Ox.
I	1.96	1.98	1.97	1.97
II	3.97	3.98	3.98	3.97
III	6.13	5.98	6.07	5.93
IV	7.95	7.95	7.93	7.95
V	–	–	10.09	10.10
VI	–	–	11.95	11.94

show that in solution, **1** reversibly accepts 8 electrons, while **2** reversibly accepts 12.[28]

Scanning electron microscopy (SEM; Figure 3a) of the perovskite surface shows full surface coverage and uniform microscale grain structure (ca. 300 nm) and no apparent pinholes, allowing uniform layers of **1** or **2** to be spin cast on top of this layer. Additionally, the cross-section in Figure 3b clearly shows the uniformity of each layer. The perovskite layer was also analyzed by X-ray diffraction (XRD). The Supporting Information, Figure S3, shows diffraction peaks located at 2θ for a pure perovskite material with no presence of PbI_2 or CH_3NH_2I.

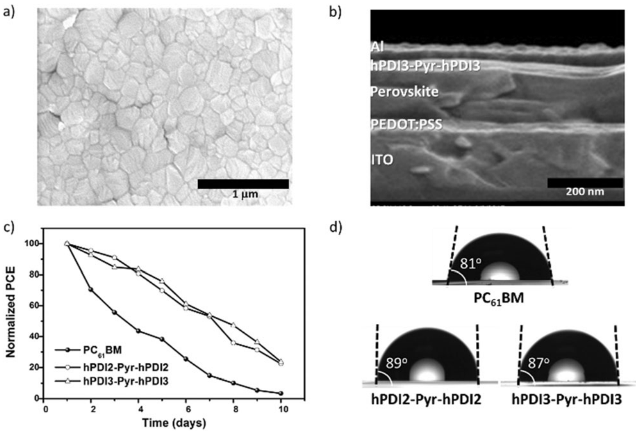

Figure 3. a) Top-view SEM image of $CH_3NH_3PbI_3$ deposited on PEDOT:PSS. b) Cross-section SEM image of an inverted PSC. c) Normalized PCE of PSCs measured as a function of the time in circa 15% humidity at room temperature. d) Images of the water droplet contact angles on the surfaces of $PC_{61}BM$, hPDI2-Pyr-hPDI2, and hPDI3-Pyr-hPDI3 thin films.

Finally, the stability of un-encapsulated devices based on **1**, **2**, and $PC_{61}BM$ as the ETMs was monitored for 10 days at room temperature with a relative humidity of approximately 15%. As shown in Figure 3c, the devices based on the two ribbons showed a slightly higher stability than those based on $PC_{61}BM$. After 10 days, the devices based on $PC_{61}BM$ were completely degraded and showed a PCE decrease of 99%. However, the devices based on **1** and **2** under the same conditions kept around 20% of their initial PCE.

The Supporting Information, Figure S4, shows efficiencies for devices fabricated using $PC_{61}BM$, **1** and **2** as the ETMs. Whereas $PC_{61}BM$-based devices exhibit rapidly decreasing efficiencies owing to the fast decrease of FF values, compounds **1**- and **2**-based devices show gradually decreasing FF as well as J_{sc} and V_{oc} values. To understand this behavior, contact angles of water droplets on perovskite/**1**, perovskite/**2**, and perovskite/$PC_{61}BM$ were measured resulting in values of 89°, 87°, and 81°, respectively, as shown in Figure 3d. These values indicate that **1** and **2** are slightly more hydrophobic than $PC_{61}BM$, therefore improving the long-term device stability. Unlike $PC_{61}BM$, the nanoribbon sidechains can be easily modified to provide additional stability.

In conclusion, two atomically precise graphene nanoribbons were used as efficient ETMs in inverted PSCs. Devices based on the two nanoribbons showed higher PCEs than devices based on $PC_{61}BM$, with negligible hysteresis in all cases. The long-term device stability was also improved when **1** or **2** were used as the ETMs. Our results show that graphene nanoribbons can be efficient electron-transport layers for PSCs and provide an alternative platform from $PC_{61}BM$. The ease of control of the electronic structure and hydrophobicity of these graphene nanoribbons could lead to further optimization of both the device stability and PCE in PSCs, which is currently ongoing in our lab.

Acknowledgements

L.E. thanks the US National Science Foundation (NSF) for generous support under the NSF-PREM program (DMR 1205302) and the CHE-1408865. The Robert A. Welch Foundation is also gratefully acknowledged for an endowed chair to L.E. (Grant AH-0033). C.N. thanks the Office of Naval Research for support under award no. N00014-16-1-2921. X.-Y.Z. and C.N. acknowledge support by the U.S. Department of Energy grant DE-SC0014563 for the spectroscopy experiments. C.N. thanks Sheldon and Dorothea Buckler for their generous support. S.P. was supported by the Department of Defense (DoD) through the National Defense Science & Engineering Graduate Fellowship (NDSEG) Program.

Conflict of interest

The authors declare no conflict of interest.

Keywords: electron-transporting materials · nanoribbons · perovskite · photoluminescence · solar cells

---

[1] Y. Zhao, K. Zhu, *Chem. Soc. Rev.* **2016**, *45*, 655.
[2] M. Ye, X. Hong, F. Zhang, X. Liu, *J. Mater. Chem. A* **2016**, *4*, 6755.
[3] A. Kojima, K. Teshima, Y. Shirai, T. Miyasaka, *J. Am. Chem. Soc.* **2009**, *131*, 6050.
[4] Best Research-Cell Efficiencies, http://www.nrel.gov/pv/assets/images/efficiency_chart.jpg, (accesed:June 2017).
[5] E. L. Ratcliff, B. Zacher, N. R. Armstrong, *J. Phys. Chem. Lett.* **2011**, *2*, 1337.

[6] S. Yang, W. Fu, Z. Zhang, H. Chen, C.-Z. Li, *J. Mater. Chem. A* **2017**, *5*, 11462.

[7] K. T. Cho, S. Paek, G. Grancini, C. Roldan-Carmona, P. Gao, Y. Lee, M. K. Nazeeruddin, *Energy Environ. Sci.* **2017**, *10*, 621. 0.

[8] D. Luo, L. Zhao, J. Wu, Q. Hu, Y. Zhang, Z. Xu, Y. Liu, T. Liu, K. Chen, W. Yang, W. Zhang, R. Zhu, Q. Gong, *Adv. Mater.* **2017**, *29*, 1604758.

[9] J. H. Kim, S. T. Williams, N. Cho, C.-C. Chueh, A. K. Y. Jen, *Adv. Energy Mater.* **2015**, *5*, 1401229.

[10] Y. Deng, E. Peng, Y. Shao, Z. Xiao, Q. Dong, J. Huang, *Energy Environ. Sci.* **2015**, *8*, 1544.

[11] C.-C. Chueh, C.-Z. Li, A. K. Y. Jen, *Energy Environ. Sci.* **2015**, *8*, 1160.

[12] C. Tian, E. Castro, T. Wang, G. Betancourt-Solis, G. Rodriguez, L. Echegoyen, *ACS Appl. Mater. Interfaces* **2016**, *8*, 31426.

[13] C. Tian, K. Kochiss, E. Castro, G. Betancourt-Solis, H. Han, L. Echegoyen, *J. Mater. Chem. A* **2017**, *5*, 7326.

[14] E. Castro, G. Zavala, S. Seetharaman, F. D'Souza, L. Echegoyen, *J. Mater. Chem. A* **2017**, *5*, 19485.

[15] S. Collavini, I. Kosta, S. F. Völker, G. Cabanero, H. J. Grande, R. Tena-Zaera, J. L. Delgado, *ChemSusChem* **2016**, *9*, 1263.

[16] T. Gatti, E. Menna, M. Meneghetti, M. Maggini, A. Petrozza, F. Lamberti, *Nano Energy*, DOI: https://doi.org/10.1016/j.nanoen.2017.09.016.

[17] R. Sandoval-Torrientes, J. Pascual, I. García-Benito, S. Collavini, I. Kosta, R. Tena-Zaera, N. Martín, J. L. Delgado, *ChemSusChem* **2017**, *10*, 2023.

[18] D. Zhao, Z. Zhu, M.-Y. Kuo, C.-C. Chueh, A. K. Y. Jen, *Angew. Chem. Int. Ed.* **2016**, *55*, 8999; *Angew. Chem.* **2016**, *128*, 9145.

[19] C. Sun, Z. Wu, H.-L. Yip, H. Zhang, X.-F. Jiang, Q. Xue, Z. Hu, Z. Hu, Y. Shen, M. Wang, F. Huang, Y. Cao, *Adv. Energy Mater.* **2016**, *6*, 1501534.

[20] Z. Zhu, C.-C. Chueh, G. Zhang, F. Huang, H. Yan, A. K. Y. Jen, *ChemSusChem* **2016**, *9*, 2586.

[21] P.-Y. Gu, N. Wang, C. Wang, Y. Zhou, G. Long, M. Tian, W. Chen, X. W. Sun, M. G. Kanatzidis, Q. Zhang, *J. Mater. Chem. A* **2017**, *5*, 7339.

[22] Y. Zhong, M. T. Trinh, R. Chen, G. E. Purdum, P. P. Khlyabich, M. Sezen, S. Oh, H. Zhu, B. Fowler, B. Zhang, W. Wang, C.-Y. Nam, M. Y. Sfeir, C. T. Black, M. L. Steigerwald, Y.-L. Loo, F. Ng, X. Y. Zhu, C. Nuckolls, *Nat. Commun.* **2015**, *6*, 8242.

[23] T. J. Sisto, Y. Zhong, B. Zhang, M. T. Trinh, K. Miyata, X. Zhong, X. Y. Zhu, M. L. Steigerwald, F. Ng, C. Nuckolls, *J. Am. Chem. Soc.* **2017**, *139*, 5648.

[24] P. Schulz, E. Edri, S. Kirmayer, G. Hodes, D. Cahen, A. Kahn, *Energy Environ. Sci.* **2014**, *7*, 1377.

[25] Y. Shao, Y. Yuan, J. Huang, *Nat. Energy* **2016**, *1*, 15001.

[26] J. You, Z. Hong, Y. Yang, Q. Chen, M. Cai, T.-B. Song, C.-C. Chen, S. Lu, Y. Liu, H. Zhou, *ACS Nano* **2014**, *8*, 1674.

[27] P.-W. Liang, C.-Y. Liao, C.-C. Chueh, F. Zuo, S. T. Williams, X.-K. Xin, J. Lin, A. K. Y. Jen, *Adv. Mater.* **2014**, *26*, 3748.

[28] S. K. Lee, Y. Zu, A. Herrmann, Y. Geerts, K. Müllen, A. J. Bard, *J. Am. Chem. Soc.* **1999**, *121*, 3513.

Manuscript received: July 6, 2017
Accepted manuscript online: September 26, 2017
Version of record online: ■■ ■■, ■■■■

Zuschriften

Solarenergiematerialien

E. Castro, T. J. Sisto, E. L. Romero, F. Liu, S. R. Peurifoy, J. Wang, X. Zhu, C. Nuckolls,* L. Echegoyen* ______ ■■■■–■■■■

Cove-Edge Nanoribbon Materials for Efficient Inverted Halide Perovskite Solar Cells

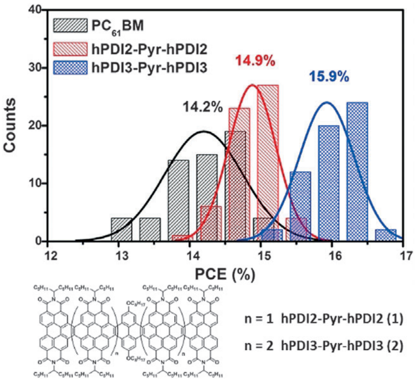

Blaue Nanobänder-Solarzellen: Zwei elektronenarme Graphen-Nanobänder werden als Elektronentransportmaterialien (ETMs) in invertierten Perowskit-Solarzellen (PSCs) genutzt und zeigen höhere Leistungen als das übliche $PC_{61}BM$. Die wichtigsten Vorteile sind der höhere Wirkungsgrad (>10% als $PC_{61}BM$) und die längere Lebensdauer der Zelle, die den hydrophoben Alkylketten in den Bändern zu verdanken ist.